A Study of Integrated Low-Permittivity Lenses With Strong Shadow Region Illumination

Dunja Lončarević, *Graduate Student Member, IEEE*, Martí Xargay Ferrer, *Graduate Student Member, IEEE*, Huasheng Zhang, *Member, IEEE*, Andrea Neto, *Fellow, IEEE*, and Nuria Llombart, *Fellow, IEEE*

***Abstract*—This article investigates the validity of the physical optics/geometrical optics (PO/GO) approximation in modeling low-permittivity integrated lens antennas when there is significant illumination of the shadow region as a function of the feed and lens geometry. The comparative analysis reveals that for certain extended hemispherical lenses, feed illumination of the lens surface beyond the critical angle leads to significant discrepancies in radiation pattern and antenna gain between PO/GO predictions and full-wave simulations. These discrepancies are traced to the constructive far-field contribution of the shadow region currents relative to those originating from the top lens region below the critical angle. The measurements of fabricated extended hemispherical lenses confirm these findings, showing up to 2-dB gain enhancement over PO/GO predictions and showcasing the limitations of traditional high-frequency modeling techniques in capturing this phenomenon. The significant gain enhancement, along with the clean measured radiation patterns, highlights the potential of using lens antenna designs with feeds that provide strong shadow region illumination. These findings provide new insights into the development of high-performance integrated lens antennas for advanced communication and sensing applications.**

***Index Terms*—Critical angle, geometrical optics (GO), integrated lens antenna, low-permittivity lens, near-field measurements, physical optics (PO), shadow region.**

I. Introduction

LENS antennas have attracted significant attention in recent years due to their ability to offer high gain, wide bandwidth, and precise beam shaping, making them crucial for emerging communication networks such as 5G, 6G, and beyond [1], [2], [3], [4]. Their potential is further amplified by the ability to integrate feeds directly into the lens structure, improving performance and enabling more compact designs [5], [6], [7]. In addition to their role in future wireless systems, lens antennas have demonstrated great versatility in applications such as radar systems, imaging technologies, and satellite communications, driving continuous innovation in their design and optimization [8], [9], [10].

The stringent requirements of future telecommunication systems, often demanding a directivity of 30 dBi or higher, lead to large lens diameters, sometimes reaching up to 30 wavelengths. For such applications, low-permittivity plastics are a viable candidate for the lens material, due to their low-loss properties, which help maintain efficiency even at higher frequencies [8]. Designing such high-directivity lenses with integrated feeds using commercial full-wave simulation tools is both computationally intensive and time-consuming. To address these challenges, designers commonly rely on the approximations provided by physical optics/geometrical optics (PO/GO) models [11], [12], [13], [14], [15]. In this approach, GO is used to model propagation inside the lens, while the far-field is computed by radiating equivalent currents on the lens surface based on the PO approximation and the equivalence theorem.

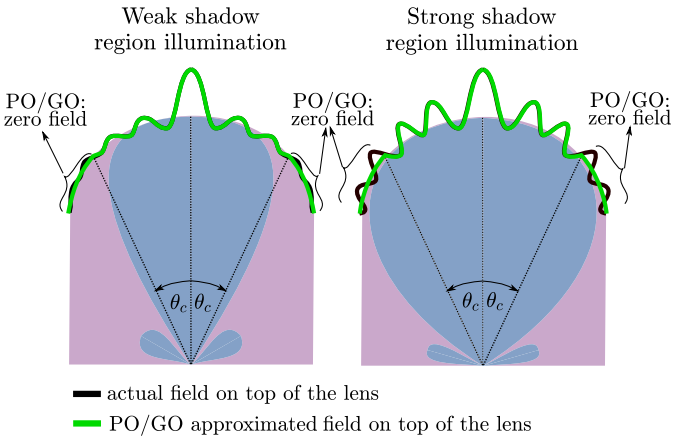

Fig. 1. Difference between the PO/GO approximated field and the actual field on top of the lens surface. Geometry with a weakly illuminated shadow region (left). Geometry with a strongly illuminated shadow region (right). Angle at which the critical angle occurs is denoted with θ_c. Blue color represents the radiation pattern of the feed.

Particularly of interest for this article is the approximation of zero-field beyond the critical angle, creating a shadow region. As illustrated in Fig. 1, depending on the feed's illumination level of this shadow region, the validity of the PO/GO approximation is expected to vary. When the shadow region is strongly illuminated, the resulting error in the field distribution on the lens surface is more significant than in cases of weak illumination. While the limitations of this critical angle approximation have been analyzed primarily in terms of numerical accuracy [16], [17], its design implications remain unexplored. This is primarily because lens feeds are typically designed to avoid significant illumination of the lens

Received 14 February 2025; revised 4 September 2025; accepted 27 September 2025. Date of publication 10 October 2025; date of current version 21 January 2026. *(Corresponding author: Dunja Lončarević.)*

The authors are with the Terahertz Sensing Group, Delft University of Technology, 2628 CD Delft, The Netherlands (e-mail: d.loncarevic@tudelft.nl; m.xargayferrer@student.tudelft.nl; h.zhang-12@tudelft.nl; a.neto@tudelft.nl; n.llombartjuan@tudelft.nl).

Digital Object Identifier 10.1109/TAP.2025.3618091

surface beyond the critical angle, minimizing the impact of this approximation in traditional designs. Furthermore, to the best of the authors' knowledge, no experimental demonstration of an efficient lens design with a strongly illuminated shadow region has been provided to date.

In this article, the effect of strongly illuminating the shadow region of the lens is studied numerically and experimentally for an extended hemispherical lens of different diameters and extension lengths. Since the commercially available full-wave tools are limited in terms of the lens size that can be simulated, this study is first conducted for a lens in a parallel-plate waveguide (PPW) environment for both TM and TE incidence, with the results being related to the 3-D lens antenna. Furthermore, experimental results for extended hemispherical lenses of different diameters with a strongly illuminated shadow region are given in this article for the first time, not only verifying the limitation of the PO/GO model, but also showing a significantly higher measured gain than the PO/GO model predicts.

This work adopts a structured methodology to evaluate the accuracy of the PO/GO approximation across increasingly complex simulation and measurement setups. Section II begins with the analysis of 2-D lenses in a PPW configuration, which enables efficient and isolated evaluation of the impact of lens geometry and shadow region illumination under both TE and TM incidence. This controlled environment allows direct comparison between full-wave simulations and PO/GO predictions and facilitates decomposition of the far-field into contributions from regions below and above the critical angle. In Section III, these insights are extended to 3-D integrated lenses using full-wave simulations of geometries equivalent to those studied in the PPW case. Section IV presents experimental near-field measurements of fabricated lens prototypes, from which the far-field is reconstructed and compared to PO/GO predictions. This multilevel approach enables consistent evaluation of the PO/GO approximation across simulation and measurement domains and highlights conditions under which it becomes inaccurate. Conclusions are given in Section V.

II. Validity of PO/GO for PPW Lenses

Simulating lens antennas with diameters in the order of 30 wavelengths using full-wave software tools like CST Microwave Studio [18] is either extremely time-consuming and impractical for design purposes or outright impossible due to the size of the lens. To address this challenge, high-frequency approximations such as PO/GO are often employed for lens antenna design. However, studying the validity of PO/GO approximations requires full-wave simulations as a reference for comparison. Therefore, it is essential to develop full-wave counterparts that correspond to the PO/GO approaches.

This section investigates the behavior of integrated lens antennas in a simplified 2-D environment using a PPW configuration. The PPW geometry enables efficient simulation of large-diameter lenses by restricting the analysis to a 2-D cross section, while allowing either TE or TM incidence w.r.t. the lens surface. The TE and TM incident waves correspond to the two principal planes of a 3-D lens, which experiences both simultaneously. The PPW configuration thus serves as a simplified problem for isolating and studying the influence of the shadow region illumination under controlled excitation. By comparing full-wave and PO/GO results, this section evaluates the conditions under which the PO/GO approximation breaks down.

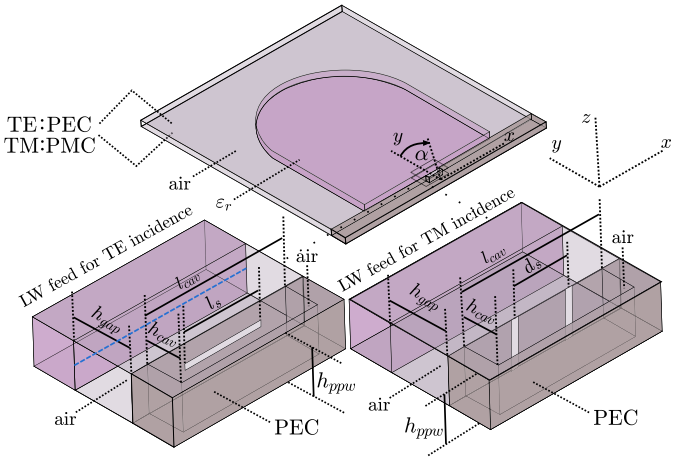

Fig. 2. Illustration of a PPW lens and its LW feed for TE and TM waves incident on the lens surface.

Contrary to the PPW lenses commonly found in the literature that radiate in free space [19], [20], the PPW lenses analyzed in this article are confined within infinite waveguide plates radiating in the PPW environment. As illustrated in Fig. 2, the lens is confined between two infinite PEC parallel plates in the case of TE incidence and between two infinite PMC plates for TM incidence. The relative permittivity of the lens is ε_r, while the rest of the PPW is filled with air. The thickness of the PPW is chosen not to support higher-order modes and is equal to $h_{ppw} = 0.25\lambda_{d,c}$, where $\lambda_{d,c}$ is the central frequency wavelength in the lens medium.

For such a defined PPW geometry, we derived a PO/GO method analogous to that used for standard 3-D lenses, starting from the Green's function of an infinite electric current radiating in a homogeneous medium. The derivation steps and resulting expressions are provided in Appendix A. In the remainder of this section, we compare the PO/GO-calculated results with full-wave (CST Microwave Studio) simulations for various PPW lenses. The CST results are obtained by calculating the equivalent surface currents on the lens (TE: (6), TM: (11)), which are then used to compute the radiated field (TE: (7), TM: (12)). While the radiation patterns of the PPW lens differ from those of 3-D lenses due to its cylindrical spreading factor, we found that the insights gained into the validity of the PO/GO approximations for the PPW lens are still applicable to 3-D lenses. This applicability is shown in Section III.

A. LW Feed

For standard lens antennas, high aperture efficiency is typically achieved by designing the feed pattern below the truncation angle of the lens to be as uniform as possible, maximizing taper efficiency. At the same time, a sharp drop in field amplitude above the truncation angle is required to

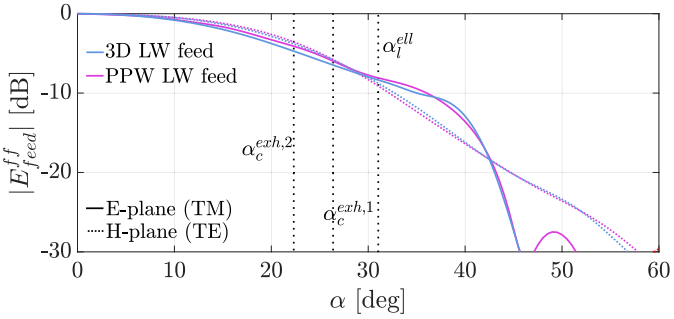

Fig. 3. PPW LW feed pattern for TM and TE incidence (Table I) compared to the 3-D LW feed pattern (Table III).

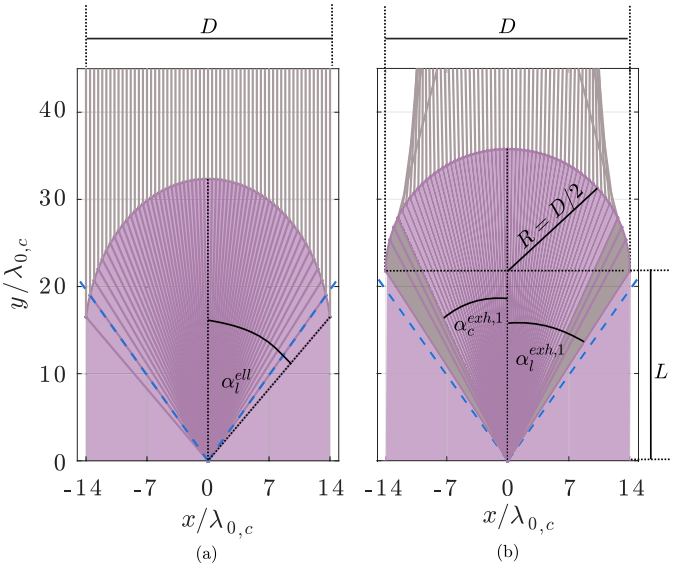

Fig. 4. (a) Elliptical lens, $\varepsilon_r = 2.19, D = 28\lambda_{0,c}$, and $\alpha_l^{ell} = 31.1°$. (b) Extended hemispherical lens, $\varepsilon_r = 2.19, D = 28\lambda_{0,c}, L_1 = 1.553R, \alpha_l^{ext,1} = 32.8°$, and $\alpha_c^{ext,1} = 25.7°$. The shadow region is indicated with the gray area.

TABLE I

GEOMETRICAL PARAMETERS OF THE PPW LW FEEDS AS ILLUSTRATED IN FIG. 2

h_{gap}	h_{cav}	l_{cav}	l_s	d_s	[unit]
0.5	0.28	1.5	0.657	0.415	$\lambda_{0,c}$

minimize spillover. This balance is often accomplished by using leaky wave (LW) antennas as feeds, which also enable seamless integration into the lens structure. The LW feed used in this work is implemented as a partially reflecting surface cavity, a configuration commonly referred to as a Fabry–Perot antenna [1], [21], [22], [23]. To maintain the PPW lens as close as possible to a 3-D lens, we choose to feed the PPW lens with a PPW LW antenna, as illustrated in Fig. 2. As can be seen, both LW feeds related to TM and TE lens' surface incidence consist of an air gap of height h_{gap} placed between the lens medium and PEC. The radiating element for the TE incidence is a thin slot of length l_s oriented along the x-axis, below which an air cavity dimensioned with h_{cav} and l_{cav} is placed to avoid back radiation. The TM incidence feed has two y-oriented slots to suppress the unwanted TM_0 mode.

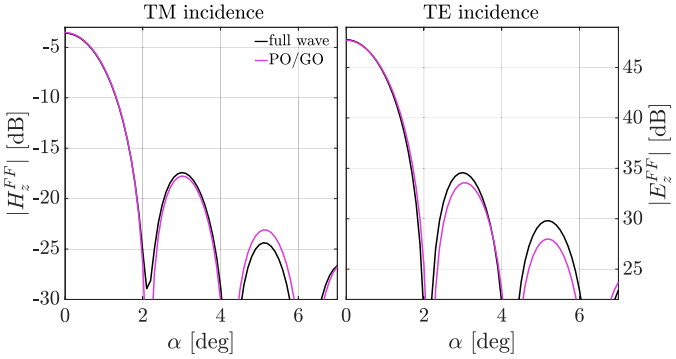

Fig. 5. PPW far-field of the elliptical lens illustrated in Fig. 4 at central frequency. Lens is fed by the TM/TE incidence LW feeds given with parameters in Table I.

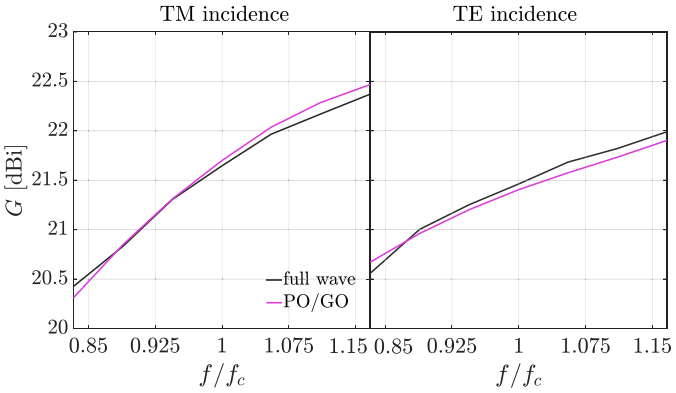

Fig. 6. PPW gain of the elliptical lens illustrated in Fig. 4. Lens is fed by the TM/TE incidence LW feeds given with parameters in Table I.

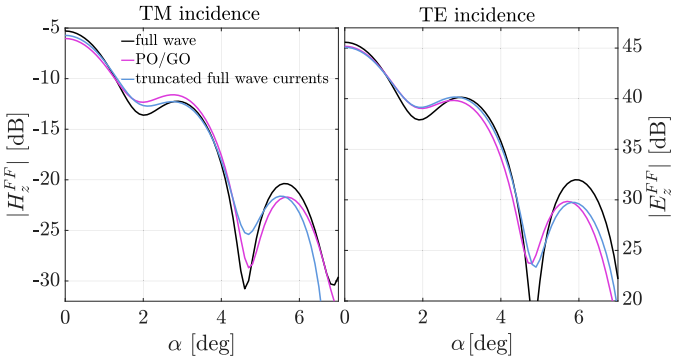

Fig. 7. PPW far-field of the extended hemispherical lens with extension $L = 1.553R$ illustrated in Fig. 4 at central frequency. Lens is fed by the TM/TE incidence LW feeds given with parameters in Table I.

TABLE II

GEOMETRICAL PARAMETERS OF THE STUDIED PPW LENSES OF DIFFERENT DIAMETERS

$D[\lambda_{0,c}]$	7	14	28
$L[R]$	1.446	1.518	1.553
α_l^{ext} [°]	34.7	33.4	32.8
α_c^{ext} [°]	28.0	26.3	25.7

To imitate the 3-D LW feed [1] used for the measurements in Section IV, LW feed parameters for both TE and TM incidence are optimized and are given in Table I for the

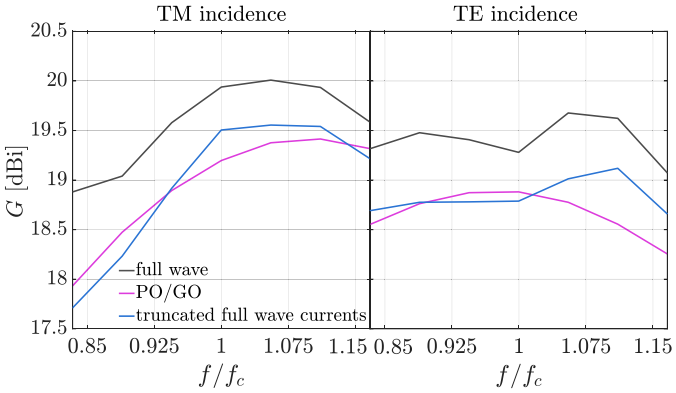

Fig. 8. PPW gain of the extended hemispherical lens with extension $L = 1.553R$ illustrated in Fig. 4. Lens is fed by the TM/TE incidence LW feeds given with parameters in Table I.

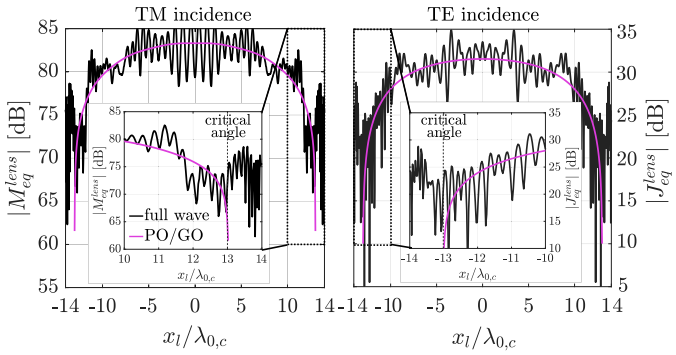

Fig. 9. Equivalent currents on top of the surface for the extended hemispherical lens with extension $L = 1.553R$ illustrated in Fig. 4 at central frequency. Lens is fed by the TM/TE incidence LW feeds given with parameters in Table I.

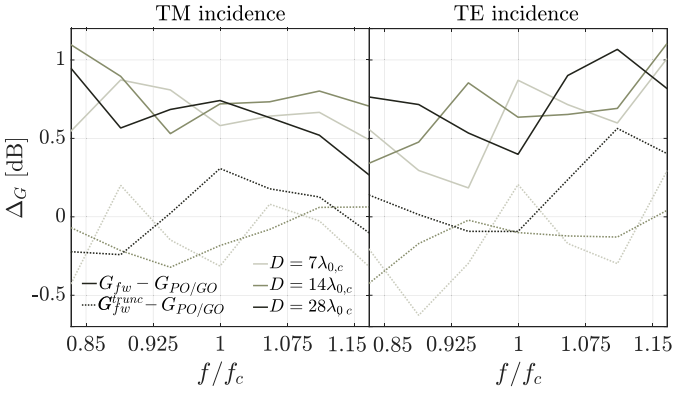

Fig. 10. Gain difference between full-wave and PO/GO models for extended hemispherical lenses of different diameters whose parameters are given in Table II. All lenses are fed by the TM/TE incidence LW feeds given with parameters in Table I.

TABLE III
GEOMETRICAL PARAMETERS OF THE 3-D LW FEED AS ILLUSTRATED IN FIG. 14

$h_{gap}[\lambda_{0,c}]$	$t[\lambda_{0,c}]$	$L_{tap}[\lambda_{0,c}]$	Φ_{tap} [°]
0.5	0.08	4.4	3
$w_g[\lambda_{0,c}]$	$w[\lambda_{0,c}]$	$\rho_0[\lambda_{0,c}]$	α [°]
0.8	0.3	0.54	65.5

HDPE lens medium of $\varepsilon = 2.19$. The radiation patterns of the optimized PPW LW feeds are presented in Fig. 3, showing

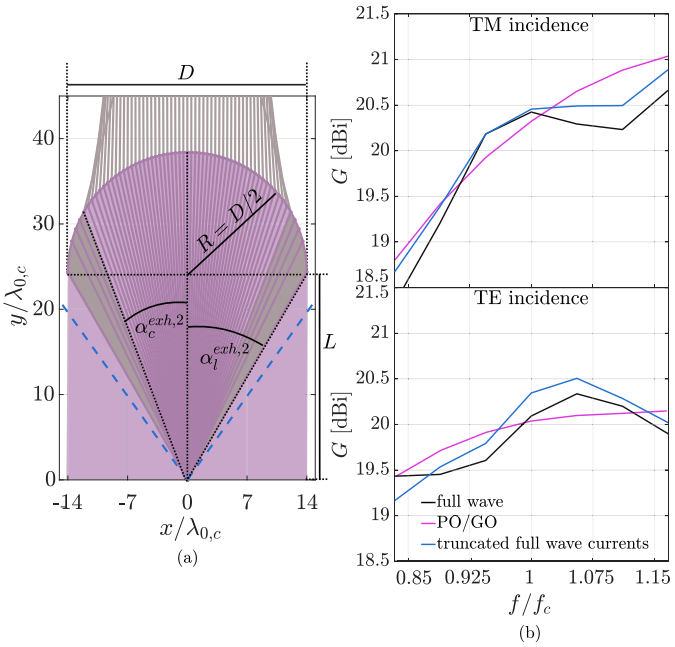

Fig. 11. (a) Extended hemispherical lens, $\varepsilon_r = 2.19, D = 28\lambda_{0,c}, L = 1.742R, \alpha_l^{ext,1} = 29.9°$, and $\alpha_c^{ext,1} = 22.7°$. The shadow region is indicated with the gray area. (b) PPW gain of the extended hemispherical lens illustrated in (a). Lens is fed by the TM/TE incidence LW feeds given with parameters in Table I.

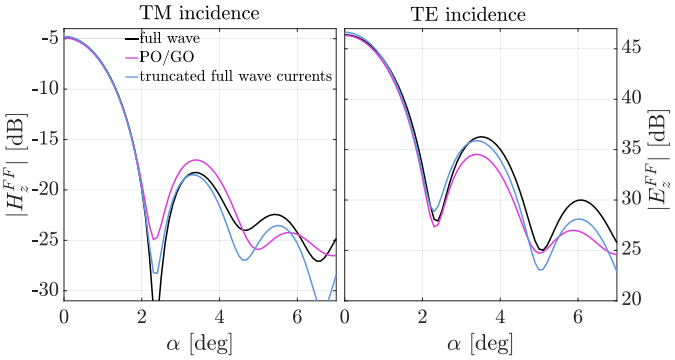

Fig. 12. PPW far-field of the extended hemispherical lens with extension $L = 1.742R$ illustrated in Fig. 4 at central frequency. Lens is fed by the TM/TE incidence LW feeds given with parameters in Table I.

an excellent agreement with the 3-D LW feed pattern in the principal planes. These PPW LW feeds are used for all lenses presented in this section.

B. Elliptical Lens

An elliptical lens is considered a canonical lens geometry since, in theory, it gives perfectly collimated beams pointing in at broadside direction. This is true, taken that the phase center of the feed is located in the lower focal point of the ellipse. An example of elliptical lens geometry for which critical angle does not appear, together with the ray tracing image is given in Fig. 4(a), where $D = 28\lambda_{0,c}$ denotes the lens diameter and $\alpha_l^{ell} = 31,1°$ its truncation angle. All the lenses presented in this article are made out of HDPE material with relative permittivity $\varepsilon_r = 2.19$, if not stated otherwise.

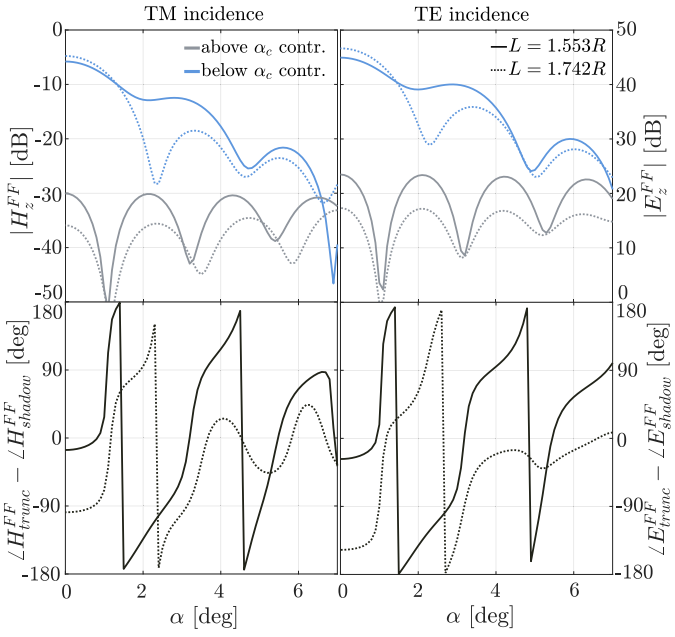

Fig. 13. PPW far-field contributions of the extended hemispherical lenses with extensions $L = 1.553R$ and $L = 1.742R$ at central frequency. Lenses are fed by the TM/TE incidence LW feeds given with parameters in Table I.

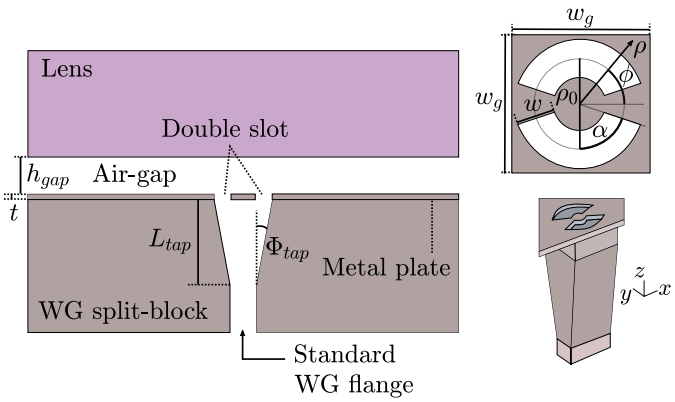

Fig. 14. Illustration of the 3-D LW feed illuminated by a square waveguide with two shaped slots as radiating elements.

Radiation patterns of the PPW elliptical lens for both incidences are plotted in Fig. 5, where the angle α is given in Fig. 2. Comparing the PO/GO and full-wave results, it can be seen that the match between the two is very good, particularly in the main beam and the first sidelobe. Similarly, the far-field gain of a cylindrical wave (Appendix) is given in Fig. 6, demonstrating good accuracy of the PO/GO approximation for the canonical case of the elliptical lens.

C. Extended Hemispherical Lens

Another commonly used lens geometry is the extended hemispherical lens [11], [24]. While elliptical lenses offer superior beam collimation and higher aperture efficiency, extended hemispherical lenses generally provide better scanning performance and are sometimes preferred as a cost-effective alternative due to their less complex geometry, which can simplify fabrication. Furthermore, the extension length of an extended hemispherical lens offers an additional degree of freedom with respect to elliptical lenses. An example of an extended hemispherical lens is shown in Fig. 4(b). Its diameter is the same as that of the elliptical lens previously introduced, and its extension L is equal to $1.553R$, where $R = D/2$ is the hemisphere's radius. Notably, for this geometry, the critical angle $\alpha_c^{ext,1} = 25.7°$ appears before the truncation angle of the lens $\alpha_l^{ext,1} = 32.8°$. Using the LW feed optimized for the elliptical lens (Fig. 3), the lens surface in the shadow region is observed to be unusually strongly illuminated.

The PPW far-field of the extended hemispherical lens is given in Fig. 7. First, it can be observed that its pattern is inferior to that of the elliptical lens plotted in Fig. 5. This is because the extension $L = 1.553R$ was chosen as the length that gives optimal performance for a 3-D extended hemispherical lens. Since the spreading factors differ, this 3-D optimal extension does not yield the best directivity and gain for the PPW lens. Second, differences between the full-wave and PPW PO/GO far-field results are visible even in the main beam, both in amplitude and shape. This discrepancy becomes more pronounced when plotting the PPW gain of the lens (Fig. 8), where deviations between the PO/GO and full-wave models range from 0.5 to 1 dB across the frequency band for both TM and TE incidence.

To better understand the difference between the PO/GO and full-wave results, the equivalent currents on the lens surface, as given in (6) for TE and (11) for TM incidence, are plotted in Fig. 9. As shown in the zoomed-in views, the PO/GO currents are abruptly truncated at the critical angle, beyond which the shadow region begins. This truncation is one of the approximations of PO/GO, which the full-wave model does not assume, allowing nonzero fields in the shadow region. To further explore the differences that occur beyond the critical angle, the PPW far-field was recalculated using full-wave equivalent currents artificially truncated at the critical angle to simulate the shadow region. The results, plotted in Figs. 7 and 8, show much better agreement between the PO/GO and the truncated full-wave models. This confirms that the primary discrepancy between the PO/GO and the full-wave arises from the shadow region, and not from the oscillations of the full-wave equivalent currents below the critical angle (related to the multiple reflections inside the lens). The results presented indicate that, for the specified geometry and feed configuration studied, the PO/GO approximation is insufficient for an accurate gain estimation.

D. Impact of the Lens Diameter

The discrepancy between the PO/GO and full-wave results was also analyzed for extended hemispherical lenses of varying diameters. The geometrical parameters of these lenses are summarized in Table II, all of which share very similar truncation and critical angles.

The differences in gain between the full-wave and PO/GO results are shown in Fig. 10. As observed, the discrepancy between the full-wave and PO/GO results remains consistent across all three lenses and does not appear to depend on the lens diameter. Additionally, following the same procedure as presented in the previous section, full-wave equivalent currents

are truncated at the corresponding critical angles from which the PPW far-fields are calculated. As can be noted from Fig. 10, the difference between such truncated results and PO/GO models is lowered for all the lenses studied, once again highlighting the validity limitation of the PO/GO model in the shadow region.

E. Impact of the Extension Length

In Sections II-C and II-D, it was shown that the specified extended hemispherical PPW lens geometry and LW feed combination result in a notable mismatch between the PO/GO approximation and the full-wave model. Further analysis by the authors revealed that this discrepancy is highly sensitive to the lens material and geometry. To illustrate this, another example is presented: an extended hemispherical lens with the same diameter and material as the lens previously studied but with a different extension length, $L = 1.742R$. Its geometry and ray tracing image are shown in Fig. 11(a), while the feeding element remains the same as in the previously studied PPW lenses.

The critical angle of this lens appears at $\alpha_c^{ext,2} = 22.7°$, and as can be seen in Fig. 3, its shadow region is illuminated even more strongly compared to the extended hemispherical lens with a shorter extension, $L = 1.553R$. However, as shown in Figs. 11 and 12, the discrepancy between the PO/GO model and full-wave results is significantly smaller for this lens. While the agreement is not as precise as in the case of the elliptical lens, the match between the two methods is relatively good, and truncating the full-wave currents has minimal impact on the radiation pattern and gain.

To further examine the impact of lens geometry on the validity of the zero-field approximation in the shadow region, the full-wave far-field is decomposed into two components.

1) $E/H^{FF}_{z,trunc}$: the contribution from equivalent currents on the lens surface below the critical angle (previously given with blue in Figs. 7 and 12).
2) $E/H^{FF}_{z,shadow}$: the contribution from the shadow region equivalent currents. The shadow region is confined between the critical angle and the truncation angle of the lens, as illustrated with gray color in Figs. 4 and 11.

The total far-field (previously given with black in Figs. 7 and 12) is equal to the summation of the two contributions

$$E/H^{FF}_{z,total} = E/H^{FF}_{z,trunc} + E/H^{FF}_{z,shadow}. \quad (1)$$

For the extended hemispherical lenses with $L = 1.553R$ and $L = 1.742R$, the amplitudes of these far-field components and their phase differences are plotted in Fig. 13. In the $L = 1.553R$ case, the shadow region contribution at broadside is approximately 20–25 dB lower than that from below the critical angle. However, for both TM and TE incidence, these components are nearly in phase, resulting in constructive summation at broadside and explaining the gain discrepancy between the PO/GO approximation and the full-wave model observed in Fig. 8.

For the $L = 1.742R$ lens, the two far-field components are nearly out of phase, resulting in a destructive summation of the fields at broadside. This is evident in the gain plots in Fig. 11, where the gain calculated from truncated full-wave currents exceeds the gain that includes both below- and above-critical-angle contributions. However, since the amplitude difference between these components is large (>30 dB), the resulting gain reduction is relatively minor. As a result, the PO/GO and full-wave models show closer agreement, as illustrated in Fig. 11.

These findings show that the accuracy of the PO/GO approximation depends not only on the illumination strength beyond the critical angle but also on the lens geometry. When the far-field contribution of the shadow region currents is negligible compared to that of the equivalent currents below the critical angle, the zero-field shadow region approximation holds. However, when the shadow region contribution to the far-field, which can be either destructive or constructive, is significant, PO/GO predictions become unreliable.

III. 3-D Integrated Lens With Strong Shadow Region Illumination

To extend the observations from the PPW analysis to realistic antenna configurations, this section presents the analysis of 3-D integrated lenses. The geometries used match those from the PPW section, allowing for consistent comparison across 2-D and 3-D lens models. By examining how the radiation characteristics and gain differ between PO/GO predictions and full-wave results, this section assesses whether the shadow region contributions observed in 2-D persist under full 3-D excitation and geometry.

Given the limitations of full-wave simulations for large lens volumes, the studied 3-D lens geometry is a $D = 14\lambda_{0,c}$ extended hemispherical lens, with its parameters listed in Table II. This 3-D lens shares the same cross section as the previously analyzed PPW lens of the same diameter. The feeding element is an LW antenna, shown in Fig. 14 and originally presented in [1]. It consists of a half-wavelength air gap between the lens medium and the PEC, with two shaped slots serving as radiating elements. These slots are excited by the TE_{10} mode of a square waveguide, which is tapered to a standard flange, as illustrated in the figure. The geometrical parameters of the LW feed are provided in Table III, and its radiation pattern in principal planes is plotted in Fig. 3. The same LW antenna is used as the feed for all lenses presented in this section and in the experimental validation section.

The PO/GO results are first compared to the full-wave model, referred to as Model A, as shown in Fig. 15(a). To account for spillover and reflected waves, absorbers with a PEC top layer are placed around the lens extension. These absorbers, which have the same permittivity as the lens and a loss tangent of $\tan\delta = 0.1$, capture this energy as ohmic losses, mimicking the PO/GO assumption that such energy is lost. As seen in Fig. 15(b), the gain difference between the PO/GO and full-wave results is significant. This discrepancy, previously observed in the PPW lens, is also evident in the far-field pattern of the 3-D lens, as shown in Fig. 16.

To further investigate this, a second full-wave model, referred to as Model B, is simulated. In Model B, the absorber with the PEC sheet is elevated to the critical angle plane as calculated from the feed's phase center. This placement of the absorber effectively forces the field in the shadow region to

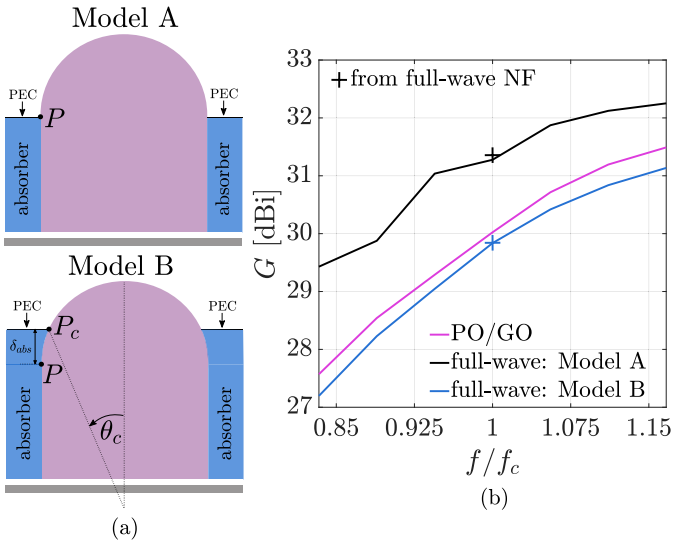

Fig. 15. (a) Cross section of the full-wave models. (b) Gain of the 3-D lens fed by the LW antenna parameterized in Table III.

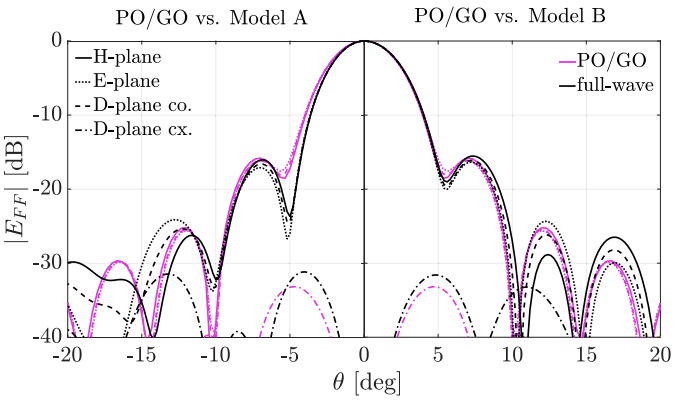

Fig. 16. Far-field of the 3-D lens fed by the LW antenna parameterized in Table III at central frequency.

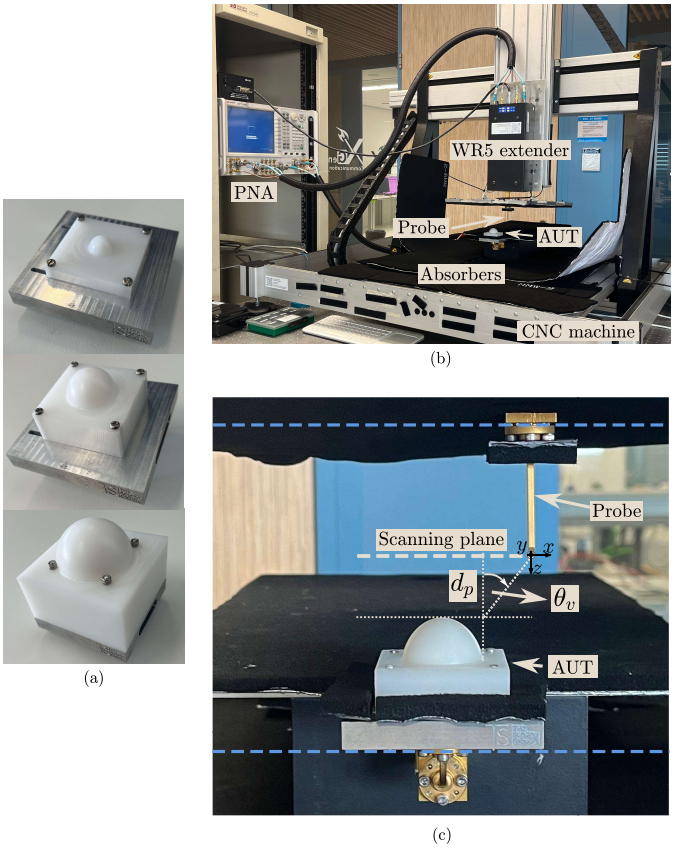

Fig. 17. (a) Fabricated lenses, from the smallest (top) to the largest (bottom) diameter. Lenses are mounted on the waveguide-based LW feed given in Fig. 14 and Table III. (b) Measurement setup. (c) Measurement setup: close-up. Dashed blue lines represent reference planes.

zero, following an approach similar to the full-wave equivalent currents truncation used for the PPW lens. As shown in the gain and far-field plots in Figs. 15(b) and 16, the agreement between Model B and PO/GO is significantly better than that between Model A and PO/GO. This confirms that the primary limitation of the PO/GO model in this case stems from its assumption of zero field beyond the critical angle.

The results presented in this section show a qualitative match between the 3-D analysis and PPW results from Section II. Furthermore, the findings presented indicate that, for the studied geometry and feed configuration, PO/GO significantly underestimates antenna gain. Relying solely on this model would lead to the premature exclusion of extended hemispherical lenses with a strongly illuminated shadow region from design considerations. However, full-wave simulations reveal that such antennas can not only achieve high gain but also maintain clean radiation patterns, making them viable candidates for advanced antenna designs.

IV. Experimental Validation

For electrically large lenses, such as the $28\lambda_0$ diameter case considered in the article, full-wave simulations become computationally unfeasible. As a result, antenna measurements are necessary to evaluate the accuracy of PO/GO modeling for 3-D lenses. This section presents near-field measurements of fabricated integrated lens antennas to provide experimental validation of the PO/GO predictions. The measured lenses share the same geometries as those analyzed in the simulation sections. Far-field patterns are reconstructed from the measured near-field data and compared to PO/GO results. This comparison enables assessment of how well PO/GO captures the behavior of practical lens systems in the presence of strong shadow region illumination.

The lens results of which are presented in this section were fabricated using an in-house five-axis computer numerical control (CNC) milling machine. These lenses operate at a central frequency of $f_c = 180$ GHz, with their geometries defined by the parameters listed in Table II. As shown in the table, all lenses share similar geometries, with critical angles ranging from 25.7° to 28°. Each lens is made of HDPE, a material with a previously measured permittivity of $\varepsilon_r = 2.19$ and loss tangent $\tan\delta = 3.3 \times 10^{-4}$. The lenses are fed by the waveguide-based LW feed given in Section III, and the photographs of the fabricated lenses mounted on the feed are given in Fig. 17(a).

Measurements were performed in the near-field with the setup shown in Fig. 17(b). Using the waveguide extenders (WR 5.1) to extend the operational frequency range of the

TABLE IV

MEASUREMENT PARAMETERS OF THE FABRICATED EXTENDED HEMISPHERICAL LENSES AND THE MEASURED ELLIPTICAL LENS

$D[\lambda_{0,c}]$	7	14	28	18 (elliptical)
d_p [cm]	1.0	2.0	2.5	2.0
θ_v [°]	49	49	25	45

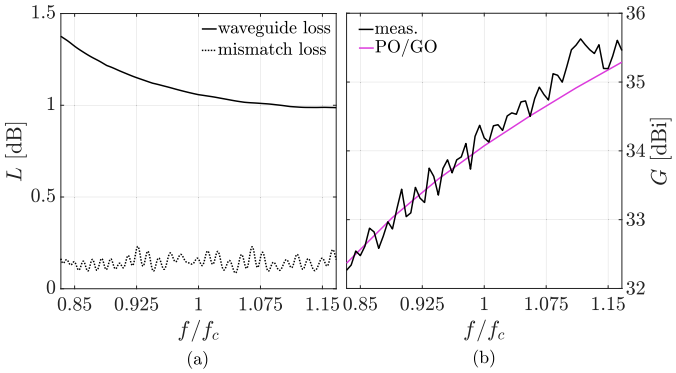

Fig. 18. (a) Mismatch and waveguide losses for the measured elliptical lens. (b) Gain of the measured elliptical lens fed by the LW feed presented in Section III.

PNA, the performance of the antenna under test (AUT) was characterized. A field probe of gain G_p, mounted on a CNC machine, was used to scan the near-field over a plane above the lens. The far-field of the AUT was obtained by applying the Fourier transform to the near-field. As shown in Fig. 17(c), the distance between the scanning plane and the surface of the lens is given with d_p, while θ_v corresponds to the angle below which the calculated far-field is valid. The geometric values for the measurements performed are given in Table IV.

The far-field gain of the measured antennas is calculated from the near-field data, as presented in Appendix B. To compare the obtained gain results to those calculated with the PO/GO model, the losses due to the port mismatch and metal roughness inside the waveguide are de-embedded. Taking (20) into account, the de-embedded measured gain is equal to

$$G\,[\mathrm{dBi}] = G'\,[\mathrm{dBi}] + L_m\,[\mathrm{dB}] + L_{wg}\,[\mathrm{dB}]\,, \tag{2}$$

where the mismatch loss is $L_m = -10\log_{10}(1-|S_{11}|^2) - 10\log_{10}(1-|S_{22}|^2)$ and the waveguide loss L_{wg} is obtained via a full-wave simulation.

A. Elliptical Lens

Before measuring the extended hemispherical lenses, an elliptical lens from [1] was measured, and its results were compared to PO/GO. This validation step ensured the accuracy of the nonstandard far-field gain calculation derived from near-field measurements, since the gain of this lens was previously measured in far-field with good alignment with PO/GO predictions [1]. The lens geometry is defined by a diameter of $D = 18\lambda_{0,c}$ and a truncation angle of 40.3° occurring below the critical angle. Its material has a measured permittivity of 2.35.

The far-field of the lens was calculated from the near-field measurements, which were time-gated to exclude the reflections caused by the measurement setup.[1] This measured radiation pattern matches well with previous measurements, and PO/GO results as given in [1]. Additionally, the gain obtained from the near-field measurements, and the waveguide and mismatch losses are shown in Fig. 18. The waveguide loss, due to the metal roughness, is significant, highlighting the need for de-embedding to accurately compare the measured gain with the PO/GO result. After de-embedding, the measured gain aligns well with the PO/GO prediction, confirming the validity of the gain extraction method and the measurement setup.

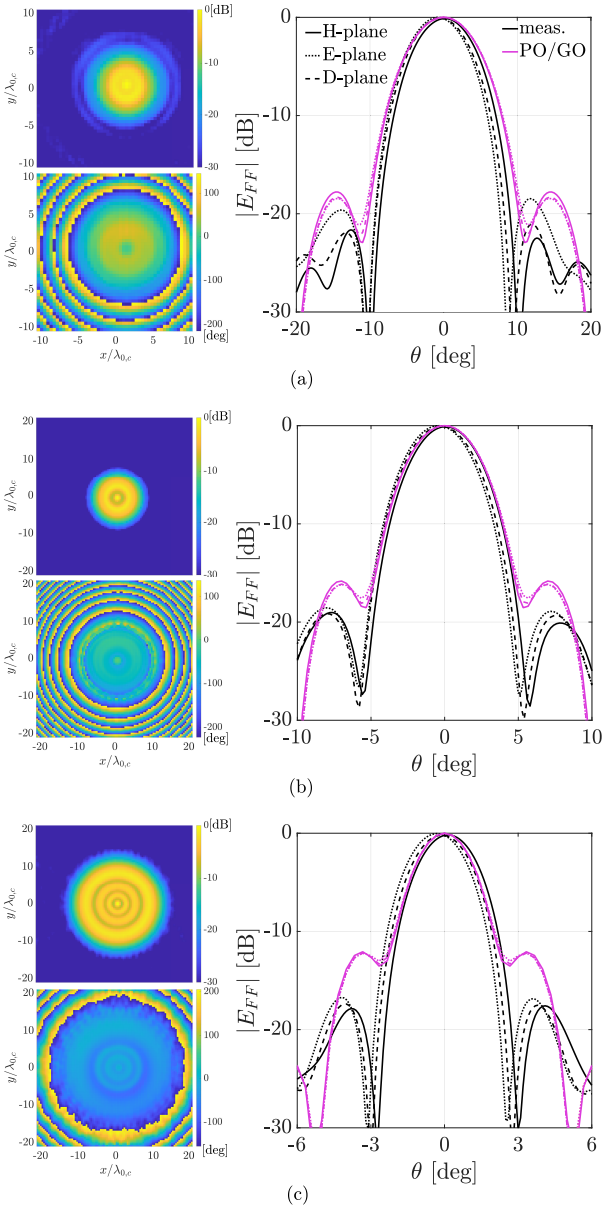

Fig. 19. Extended hemispherical lens near-field measurements at the central frequency (left). Extended hemispherical lens far-field at the central frequency (right). (a) $D = 7\lambda_{0,c}$, (b) $D = 14\lambda_{0,c}$, and (c) $D = 28\lambda_{0,c}$. Lenses are fed by the LW feed presented in Section III.

[1]It was observed that this time-gating has no significant effect on the measured gain.

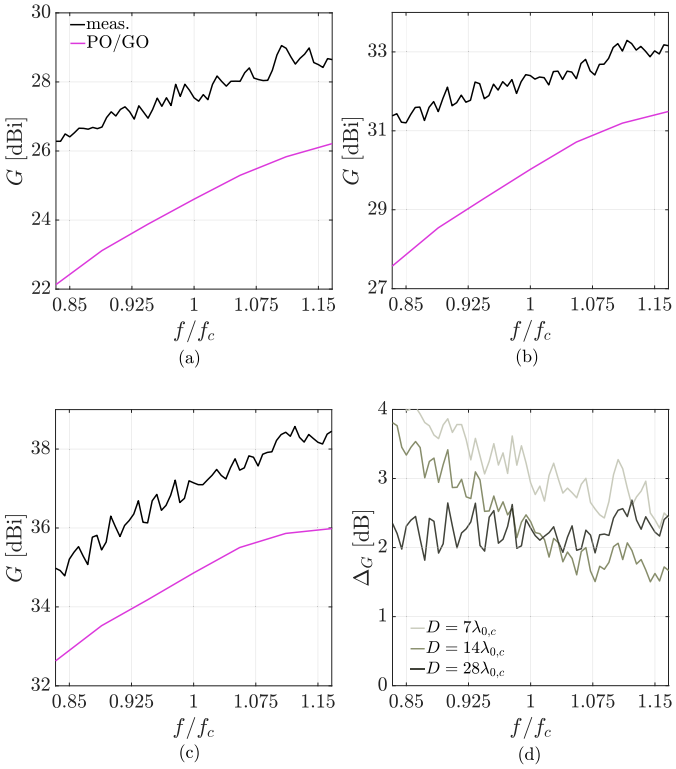

Fig. 20. (a)–(c) Extended hemispherical lens gain. (a) $D = 7\lambda_{0,c}$. (b) $D = 14\lambda_{0,c}$. (c) $D = 28\lambda_{0,c}$. (d) Difference between the measured gain and the PO/GO gain. Lenses are fed by the LW feed presented in Section III.

B. Extended Hemispherical Lenses

The near-field measurements and radiation patterns for the three extended hemispherical lenses are shown in Fig. 19. As anticipated from the full-wave results in Section III, the measured radiation patterns for the lenses with strong illumination beyond the critical angle remain exceptionally clean. Notably, their sidelobes are lower than those predicted by the PO/GO model, with the largest lens exhibiting a difference of approximately 7 dB in the sidelobes.

The measured (de-embedded) gains are plotted in Fig. 20(a)–(c), while Fig. 20(d) highlights the significant discrepancies between these measurements and the PO/GO results. It can be noted that the deviation for the two smaller lenses is frequency-dependent, being larger for the $D = 7\lambda_{0,c}$. However, for the largest lens, this discrepancy, much like the critical angle itself, is frequency-invariant and is around 2 dB. The highlighted discrepancies between the PO/GO and measured results indicate that the shadow region currents add constructively to the far-field of the lenses for all measured diameters. Most interestingly, for the $D = 28\lambda_{0,c}$ lens, this constructive contribution leads to a significant aperture efficiency difference between the PO/GO, 40%, and the measurements, 67%.

While previous work, such as [16], has proposed a method to recover the field radiated by shadow region currents, it did not provide practical insight into how shadow region illumination contributes to the far-field or the design implications it might have. In this article, by decomposing the far-field into contributions from below and beyond the critical angle, it is shown that shadow region currents can interfere either constructively or destructively with the rest of the radiated field, depending on the lens geometry and illumination conditions. This observation helps clarify when and why the PO/GO approximation breaks down in certain configurations. While this study focuses on extended hemispherical lenses, the results highlight the importance of accounting for shadow region effects in high-frequency models. A broader investigation across different lens geometries and feed configurations is needed to generalize these findings and could ultimately lead to design guidelines indicating when the PO/GO method—which remains significantly faster than full-wave [25] or hybrid approaches—can be reliably used in lens antenna design, and when it cannot.

V. Conclusion

Building on simulation-based analysis, this study presented the first experimental validation of extended hemispherical lens antennas under strong shadow region illumination, revealing notable deviations from conventional PO/GO predictions. The results indicate that, contrary to traditional lens antenna design guidelines, strong illumination beyond the critical angle does not necessarily degrade radiation performance. Instead, as shown for the lens geometry analyzed, if the shadow region currents add constructively to the far-field, it can lead to high measured gains and clean radiation patterns, suggesting that such illumination may not always be detrimental in lens antenna designs.

A key observation is that in the studied cases, due to the zero-field approximation beyond the critical angle, the PO/GO model can underestimate the gain of these lenses. The measured gain enhancements, reaching up to 2 dB over PO/GO predictions for the 28-wavelength lens, indicate that lenses with strongly illuminated shadow regions may still be viable for certain applications. This effect was validated for multiple lens diameters, for both parallel-plate waveguide and 3-D integrated lenses, reinforcing the relevance of the observed phenomenon. However, the geometrical and material sensitivity of the constructive shadow region addition to the below-critical-angle contribution, should be taken into account.

Given the increasing demand for high-directivity lens antennas in advanced communication and sensing applications, these findings suggest that further exploration of lens designs incorporating strong shadow region illumination could be beneficial. While additional studies are needed to fully characterize this effect across different configurations and the wave mechanisms behind it, the results presented here provide useful insights for optimizing future integrated lens antenna designs.

Appendix
PO/GO for PPW Derivation

In this appendix, the derivation of the PO/GO approximation is given for a PPW lens. The derivation is presented for both the TE and TM incidence, followed by the derivation of the expression for the far-field gain of a cylindrical wave.

A. TE Incidence

To facilitate PPW feeds that have current distributions that are nonanalytical, the inclusion of the feed into this model is

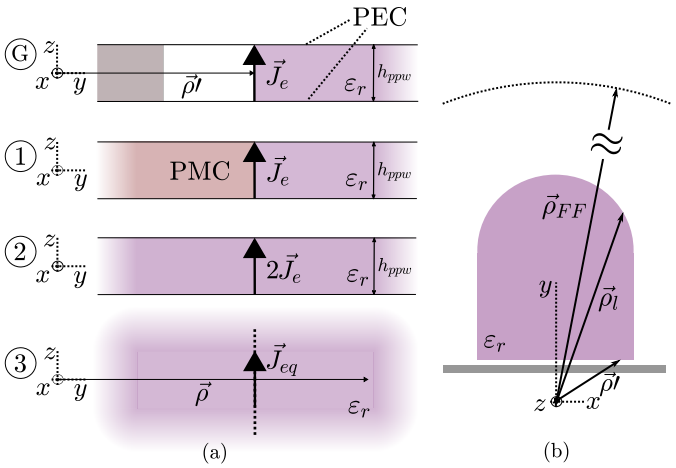

Fig. 21. (a) Visual representation of the PPW derivation steps: (G) Geometry cross section: 1) applying the PMC formulation equivalence theorem; 2) applying the image theorem with respect to the PMC plane; and 3) applying the image theorem with respect to PPW walls. (b) Coordinate system used.

done by first building a full-wave simulation of the PPW feed itself. In the case of the PPW LW feed from Fig. 2(left), the model is created to be sufficiently wide in x-direction to not truncate the feed's current distribution and with electric boundaries acting as PEC PPW plates. The background medium is set to ε_r to mimic the radiation into the lens medium, approximating that the transition from the lens to the air medium does not influence the radiation of the feed. Obtaining the full-wave results and assuming that the field across the height of the PPW is constant, the magnetic field along the top of the air-gap is taken, as shown with a blue dashed line in Fig. 2. This magnetic field is denoted with $H_{fw}^{gap}(\vec{\rho}\prime)$, where $\vec{\rho}\prime = x'\hat{x} + y'\hat{y}$ corresponds to the position on top of the gap. The yz cross section of the PPW feed and the following steps of applying electromagnetic theorems are illustrated in Fig. 21(a). First, the equivalence theorem is utilized and the space below the top of the air-gap is filled with PMC, with the equivalent electric current equal to $\vec{J}_e(\vec{\rho}\prime) = \hat{y} \times \vec{H}_{fw}^{gap}(\vec{\rho}\prime)$. Next, an image theorem can be leveraged, leading to the doubling of the equivalent electric current as noted in Step 2. Finally, after applying the image theorem an infinite number of times with respect to the PEC PPW plates, the final equivalent current distribution $\vec{J}_{eq} = 2\vec{J}_e$ is obtained. This z-oriented current extends infinitely in the same direction, radiating in the infinite medium of permittivity ε_r. [26]

The Green's function of an elementary infinite line electric current oriented along the axis in which it extends, $\vec{J}(\vec{\rho}\prime) = I_z\delta(\vec{\rho}\prime)\hat{z}$, is known in closed-form [27]

$$\vec{E}\left(\vec{\rho}\right) = \frac{k_0\zeta_0}{4} I_z H_0^{(2)}\left(k_0\sqrt{\varepsilon_r}|\vec{\rho} - \vec{\rho}\prime|\right) \tag{3}$$

where k_0 and ζ_0 are the propagation constant and the characteristic impedance of free-space, $\vec{\rho}$ is the location of the observation point, $\vec{\rho}\prime$ is the source location, and ε_r is the relative permittivity of the medium in which the current lies. The Hankel function of the second kind and zeroth-order is denoted with $H_0^{(2)}$, and it introduces the cylindrical spreading $\sqrt{\rho}$ into the PPW field. Using (3), the field incident on the surface of the PPW lens can be calculated as

$$\vec{E}_i\left(\vec{\rho}_l\right) = \hat{z}\frac{k_0\zeta_0}{4}\int_{x_{g,min}}^{x_{g,max}} \vec{J}_{eq}\left(\vec{\rho}\prime\right) H_0^{(2)}\left(k_0\sqrt{\varepsilon_r}|\vec{\rho}_l - \vec{\rho}\prime|\right) dx' \tag{4}$$

where $\vec{\rho}_l$ is the location of the point on the lens surface [Fig. 21(b)], and $x_{g,min/max}$ are the spatial limits of the current distribution along the air-gap top.

The transmitted field on top of the lens surface can be obtained by locally approximating the lens surface as flat and using the Fresnel TE transmission coefficient $\tau_{TE}(\vec{\rho}_l)$. The transmitted magnetic field on the lens surface is calculated as

$$\vec{H}_t\left(\vec{\rho}_l\right) = \frac{1}{\zeta_0}\tau_{TE}\left(\vec{\rho}_l\right) E_i\left(\vec{\rho}_l\right)\hat{s}_t\left(\vec{\rho}_l\right) \times \hat{z} \tag{5}$$

where $\hat{s}_t(\vec{\rho}_l)$ is the propagation direction of the transmitted field. It should be noted that the field beyond the critical angle, as dictated by the permittivity of the lens, is equal to zero.

Finally, the equivalence theorem with the PMC formulation can be leveraged once again, together with the image theorem applied locally, with the new equivalent electric current being equal to

$$\vec{J}_{eq}\left(\vec{\rho}_l\right) = 2\hat{n}_l\left(\vec{\rho}_l\right) \times \vec{H}_t\left(\vec{\rho}_l\right) \tag{6}$$

where $\hat{n}_l(\vec{\rho}_l)$ is the normal to the lens surface. The electric field radiated by the lens in the observation point $\vec{\rho}_{FF}$ is given with

$$\vec{E}_l\left(\vec{\rho}_{FF}\right) = \hat{z}\frac{k_0\zeta_0}{4}\int_{x_{l,min}}^{x_{l,max}} \vec{J}_{eq}\left(\vec{\rho}_l\right) H_0^{(2)}\left(k_0|\vec{\rho}_{FF} - \vec{\rho}_l|\right) |Jac\left(\vec{\rho}_l\right)| dx_l \tag{7}$$

where $x_{l,min/max}$ are the x-axis limits and $|Jac(\vec{\rho}_l)|$ the Jacobian of the lens surface.

B. TM Incidence

The steps for the derivation of the TM incidence are dual. Extracting the full-wave electric field on top of the air-gap $\vec{E}_{fw}^{gap}(\vec{\rho}\prime)$, and applying the equivalence theorem, the equivalent magnetic current is equal to $\vec{M}_e(\vec{\rho}\prime) = -\hat{y} \times \vec{E}_{fw}^{gap}(\vec{\rho}\prime)$. After utilizing the PMC equivalence theorem formulation and image theorem on all the PMC surfaces, the final equivalent magnetic current is infinitely extended in z-direction $\vec{M}_{eq} = 2\vec{M}_e$. Dual to (3)

$$\vec{H}\left(\vec{\rho}\right) = \frac{k_0\varepsilon_r}{4\zeta_0} V_z H_0^{(2)}\left(k_0\sqrt{\varepsilon_r}|\vec{\rho} - \vec{\rho}\prime|\right) \tag{8}$$

where V_z is the amplitude of the line voltage and can be used to obtain the incident magnetic field on the surface of the lens

$$\vec{H}_i\left(\vec{\rho}_l\right) = \hat{z}\frac{k_0\varepsilon_r}{4\zeta_0}\int_{x_{g,min}}^{x_{g,max}} \vec{M}_{eq}\left(\vec{\rho}\prime\right) H_0^{(2)}\left(k_0\sqrt{\varepsilon_r}|\vec{\rho}_l - \vec{\rho}\prime|\right) dx'. \tag{9}$$

The transmitted electric current below the critical angle is calculated as

$$\vec{E}_t\left(\vec{\rho}_l\right) = \frac{\zeta_0}{\sqrt{\varepsilon_r}}\tau_{TM}\left(\vec{\rho}_l\right) H_i\left(\vec{\rho}_l\right)\hat{z} \times \hat{s}_t\left(\vec{\rho}_l\right) \tag{10}$$

from which the equivalent currents on the surface of the lens can be obtained by employing the PMC equivalence theorem and image theorem

$$\vec{M}_{eq}^{l}\left(\vec{\rho}_l\right) = -2\hat{n}_l\left(\vec{\rho}_l\right) \times \vec{E}_t\left(\vec{\rho}_l\right). \tag{11}$$

Finally, the expression for the magnetic field radiated by the lens for the TM wave is given in the following form:

$$\vec{H}_l\left(\vec{\rho}_{FF}\right) = \hat{z}\frac{k_0}{4\zeta_0}\int_{x_{l,min}}^{x_{l,max}} \vec{M}_{eq}^{l}\left(\vec{\rho}_l\right) H_0^{(2)}\left(k_0|\vec{\rho}_{FF}-\vec{\rho}_l|\right)|Jac\left(\vec{\rho}_l\right)|dx_l. \quad (12)$$

C. Far-Field Gain of a Cylindrical Wave

Since the PPW lens, as presented in this article, does not radiate in the free space, the equation for the gain within the PPW environment is derived as follows. First, let us define a far-field cylinder with the radius ρ_{FF} and the azimuth angle ϕ_{FF} (Fig. 21(b)). A directivity $Dir(\phi_{FF})$ is defined as the ratio between the radiation intensity in a certain direction, $U(\phi_{FF})$, and that of an "isotropic" source, U_0. Since the power radiated by an "isotropic" PPW antenna, assuming the field invariance in z-direction, is equal to

$$P_{rad}^{iso} = \int_{-h_{ppw}/2}^{h_{ppw}/2}\int_0^{2\pi} U_0 d\phi_{FF} dz_{FF} = 2\pi U_0 h_{ppw} \quad (13)$$

the far-field directivity of a cylindrical wave can be calculated as

$$Dir\left(\phi_{FF}\right) = \frac{U\left(\phi_{FF}\right)}{P_{rad}} 2\pi h_{ppw} \quad (14)$$

with the radiation intensity for the PPW antenna that has ρ_{FF} instead of the standard squared distance, due to PPW's cylindrical spreading

$$U\left(\phi_{FF}\right) = \frac{|\vec{E}_l^{FF}\left(\phi_{FF}\right)|^2}{2\zeta_0}\rho_{FF} \quad (15)$$

where P_{rad} is the power radiated by the antenna obtained from the PPW far-field of the antenna as

$$P_{rad} = \frac{h_{ppw}}{2\zeta_0}\int_0^{2\pi} |\vec{E}_l^{FF}\left(\phi_{FF}\right)|^2 \rho_{FF} d\phi_{FF}. \quad (16)$$

The gain of the PPW lens antenna is calculated as $G(\phi_{FF}) = \eta_{rad} Dir(\phi_{FF})$, where η_{rad} is the radiation efficiency of the antenna obtained as the ratio between the power radiated as given in (16) and the power radiated by the feed calculated as

$$P_{rad}^{feed} = \frac{h_{ppw}}{2\zeta_d}\int_0^{2\pi} |\vec{E}_{feed}^{FF}\left(\phi_{FF}\right)|^2 \rho_{FF} d\phi_{FF}. \quad (17)$$

D. Calculating Far-Field Gain From Near-Field Data

This appendix introduces the nonstandard expressions used to calculate far-field gain from near-field data and validates them against full-wave results.

In a typical near-field measurement setup [Fig. 17(c)], a lens antenna is measured using a waveguide probe scanning a plane above the lens. The far-field gain can then be extracted from the near-field data. As previously suggested in [28], this can be achieved by defining near-field directivity and gain and assuming that their ratio corresponds to the far-field radiation efficiency of the antenna. Assuming a locally plane wave in the near-field of the lens, the near-field directivity of the lens can be defined using the standard formula for the directivity

$$Dir_{NF} = \frac{4\pi d_p^2}{P_{rad}}\frac{|S_{21}|^2}{2\zeta_0} \quad (18)$$

where ζ_0 is the characteristic impedance of free space and $P_{rad} = \iint_S \frac{|S_{21}|^2}{2\zeta_0} dS$ is the power radiated by the lens calculated as the power captured by the surface of the scanning plane S. Using Friss' formula, the near-field gain is calculated as

$$G_{NF} = \frac{|S_{21}|^2}{G_p}\left(\frac{4\pi d_p}{\lambda_0}\right)^2. \quad (19)$$

Finally, the far-field gain of the lens antennas is calculated as

$$G' = \eta_{rad} Dir, \quad \eta_{rad} = \frac{G_{NF}}{Dir_{NF}} \quad (20)$$

where η_{rad} is the radiation efficiency and Dir is the standard far-field directivity of the antenna, calculated from the radiation pattern. The radiation pattern is calculated from the near-field data using the Fourier transformation.

It should be noted that the presented formula for the radiation efficiency is equivalent to radiation efficiency obtained using the effective area formalism, $\eta_{rad} = \frac{\iint_S |S_{21}|^2 dS}{A_{eff}^p}$, where the effective area of the probe can be calculated as $A_{eff}^p = \frac{G_p \lambda_0^2}{4\pi}$.

E. Validation of the Gain Derived From Near-Field Data

To validate such a defined far-field gain using a full-wave lens antenna model with a single port (without the probe), $|S_{21}|^2$ needs to be calculated. The squared amplitude of the forward voltage gain can be calculated as the ratio between the power received by the (fictional) probe, P_p^{Tx}, and the power transmitted by the lens in the absence of the probe, P_l^{Tx}

$$|S_{21}|^2 = \frac{P_p^{Tx}}{P_l^{Tx}}. \quad (21)$$

Using the antenna in reception formalism to derive the expression for $|S_{21}|^2$, the open-circuit voltage reaction integral can be solved

$$V_{oc} I_0 = \iint_{S_{AA'}} \left(\vec{h}_l \cdot \vec{m}_{eq} - \vec{e}_l \cdot \vec{j}_{eq}\right) dS_{AA'} \quad (22)$$

where I_0 is the amplitude of the wanted waveguide mode in the probe when operating in transmission and $S_{AA'}$ is the cross section of the waveguide given by the waveguide dimensions a, b and $a > b$. The origin of the coordinate system adopted is at the center of the waveguide opening, with the z-axis pointing outward as noted in Fig. 17(c), and the x-axis oriented along the longer side of the waveguide cross section. The electric and magnetic field radiated by the lens in the absence of the probe are denoted with the $\vec{e}_l$ and $\vec{h}_l$. Taking only the fundamental waveguide mode, $\vec{m}_{eq} = -Z_{TE_{10}} I_0 \cos\frac{\pi x}{a}\hat{x}$ and $\vec{j}_{eq} = I_0 \cos\frac{\pi x}{a}\hat{y}$ are the equivalent magnetic and electric currents on the surface of the probe operating in transmission, where $Z_{TE_{10}} = \frac{k_0\zeta_0}{\sqrt{k_0^2-(\pi/a)^2}}$. Assuming that the field radiated by the lens is constant over the cross section of the probe opening and closing the integral, the open-circuit voltage is equal to

$$V_{oc} I_0 = -I_0 \frac{2ab}{\pi}\left(Z_{TE_{10}} h_{l,x} + e_{l,y}\right). \quad (23)$$

Power received by the probe can be calculated as

$$P_p^{Rx} = \frac{1}{2} Re\{Z_L\} |\frac{V_{oc}}{Z_L + Z_0}| \quad (24)$$

where Z_L and Z_0 are the input impedance of the load and the free-space characteristic impedance. Assuming the conjugate matching between the two and expressing $Re\{Z_L\} = \frac{2P_p^{Tx}}{|I_0|^2}$, the power received by the probe is given as

$$P_p^{Rx} = \frac{|V_{oc}I_0|^2}{16P_p^{Tx}}. \tag{25}$$

Finally, the squared amplitude of the forward voltage gain is equal to

$$|S_{21}|^2 = \frac{|V_{oc}I_0|^2}{16P_p^{Tx}P_l^{Tx}}. \tag{26}$$

To calculate the near-field gain of the lens as given in (19), the far-field gain of the probe is needed. This can be calculated from the radiation pattern obtained by radiating equivalent currents on the probe opening.

Taking the full-wave model near-field of the $D = 14\lambda_{0,c}$ extended hemispherical lens just above the top of the lens ($d_p \approx \lambda_{0,c}/3$), the radiation pattern is calculated. This pattern is practically the same as the far-field taken directly from the full-wave simulator plotted in Fig. 16(a). Additionally, far-field gain at the central frequency is calculated and plotted in Fig. 15(b), giving an excellent match with the full-wave calculated gain. The results are also plotted for the truncated full-wave model, showing similar agreement that verifies the far-field gain calculation from the near-field data.

REFERENCES

[1] M. Arias Campo, D. Blanco, S. Bruni, A. Neto, and N. Llombart, "On the use of fly's eye lenses with leaky-wave feeds for wide-band communications," *IEEE Trans. Antennas Propag.*, vol. 68, no. 4, pp. 2480–2493, Apr. 2020.

[2] Y. J. Guo, M. Ansari, R. W. Ziolkowski, and N. J. G. Fonseca, "Quasi-optical multi-beam antenna technologies for B5G and 6G mmWave and THz networks: A review," *IEEE Open J. Antennas Propag.*, vol. 2, pp. 807–830, 2021.

[3] O. Quevedo-Teruel, J. Miao, M. Mattsson, A. Algaba-Brazalez, M. Johansson, and L. Manholm, "Glide-symmetric fully metallic Luneburg lens for 5G communications at Ka-band," *IEEE Antennas Wireless Propag. Lett.*, vol. 17, no. 9, pp. 1588–1592, Sep. 2018.

[4] J. Ala-Laurinaho et al., "2-D beam-steerable integrated lens antenna system for 5G *E*-band access and backhaul," *IEEE Trans. Microw. Theory Techn.*, vol. 64, no. 7, pp. 2244–2255, Jul. 2016.

[5] A. Bisognin et al., "Ball grid array module with integrated shaped lens for 5G backhaul/fronthaul communications in F-band," *IEEE Trans. Antennas Propag.*, vol. 65, no. 12, pp. 6380–6394, Dec. 2017.

[6] H. Zhang, S. Bosma, A. Neto, and N. Llombart, "A dual-polarized 27 dBi scanning lens phased array antenna for 5G point-to-point communications," *IEEE Trans. Antennas Propag.*, vol. 69, no. 9, pp. 5640–5652, Sep. 2021.

[7] N. V. Rooijen et al., "A core-shell lens for antenna on-package integration at D-band," *IEEE Trans. Antennas Propag.*, vol. 72, no. 8, pp. 6195–6208, Aug. 2024.

[8] B. Schoenlinner, X. Wu, J. P. Ebling, G. V. Eleftheriades, and G. M. Rebeiz, "Wide-scan spherical-lens antennas for automotive radars," *IEEE Trans. Microw. Theory Techn.*, vol. 50, no. 9, pp. 2166–2175, Sep. 2002.

[9] H. Zhang, S. O. Dabironezare, J. J. Baselmans, and N. Llombart, "Focal plane array of shaped quartz lenses for wide field-of-view submillimeter imaging systems," *IEEE Trans. Antennas Propag.*, vol. 72, no. 2, pp. 1263–1274, Feb. 2024.

[10] J. J. Baselmans et al., "A kilo-pixel imaging system for future space based far-infrared observatories using microwave kinetic inductance detectors," *Astron. Astrophys.*, vol. 601, p. A89, May 2017.

[11] D. F. Filipovic, S. S. Gearhart, and G. M. Rebeiz, "Double-slot antennas on extended hemispherical and elliptical silicon dielectric lenses," *IEEE Trans. Microw. Theory Techn.*, vol. 41, no. 10, pp. 1738–1749, Oct. 1993.

[12] G. Godi, R. Sauleau, L. L. Coq, and D. Thouroude, "Design and optimization of three-dimensional integrated lens antennas with genetic algorithm," *IEEE Trans. Antennas Propag.*, vol. 55, no. 3, pp. 770–775, Mar. 2007.

[13] H. Zhang, S. O. Dabironezare, G. Carluccio, A. Neto, and N. Llombart, "A Fourier optics tool to derive the plane wave spectrum of quasi-optical systems [EM programmer's notebook]," *IEEE Antennas Propag. Mag.*, vol. 63, no. 1, pp. 103–116, Feb. 2021.

[14] I. Gashi, A. Paraskevopoulos, S. Maci, and M. Albani, "GO analysis of GRIN lens antennas by combining in a single ODE, field and wavefront-curvature transport to the ray tracing," *IEEE Trans. Antennas Propag.*, vol. 72, no. 3, pp. 2147–2160, Mar. 2024.

[15] M. Pubill-Font, F. Mesa, A. Algaba-Brazález, S. Clendinning, M. Johansson, and O. Quevedo-Teruel, "2-D ray-tracing model for multilayer dielectric dome arrays with inner reflections," *IEEE Open J. Antennas Propag.*, vol. 5, pp. 845–854, 2024.

[16] D. Pasqualini and S. Maci, "High-frequency analysis of integrated dielectric lens antennas," *IEEE Trans. Antennas Propag.*, vol. 52, no. 3, pp. 840–847, Mar. 2004.

[17] A. V. Boriskin, G. Godi, R. Sauleau, and A. I. Nosich, "Small hemielliptic dielectric lens antenna analysis in 2-D: Boundary integral equations versus geometrical and physical optics," *IEEE Trans. Antennas Propag.*, vol. 56, no. 2, pp. 485–492, Feb. 2008.

[18] *CST Microwave Studio*. Accessed: Feb. 13, 2025. [Online]. Available: https://www.cst.com

[19] F. Tokan, N. T. Tokan, A. Neto, and D. Cavallo, "The lateral wave antenna," *IEEE Trans. Antennas Propag.*, vol. 62, no. 6, pp. 2909–2916, Jun. 2014.

[20] F. Doucet, N. J. G. Fonseca, E. Girard, H. Legay, and R. Sauleau, "Analytical model and study of continuous parallel plate waveguide lens-like multiple-beam antennas," *IEEE Trans. Antennas Propag.*, vol. 66, no. 9, pp. 4426–4436, Sep. 2018.

[21] N. Llombart, G. Chattopadhyay, A. Skalare, and I. Mehdi, "Novel terahertz antenna based on a silicon lens fed by a leaky wave enhanced waveguide," *IEEE Trans. Antennas Propag.*, vol. 59, no. 6, pp. 2160–2168, Jun. 2011.

[22] S. A. Muhammad, R. Sauleau, and H. Legay, "Small-size shielded metallic stacked Fabry–Pérot cavity antennas with large bandwidth for space applications," *IEEE Trans. Antennas Propag.*, vol. 60, no. 2, pp. 792–802, Feb. 2012.

[23] S. Bosma, N. van Rooijen, M. Alonso-delPino, and N. Llombart, "A wideband leaky-wave lens antenna with annular corrugations in the ground plane," *IEEE Antennas Wireless Propag. Lett.*, vol. 21, no. 8, pp. 1649–1653, Aug. 2022.

[24] M. Alonso-delPino, C. Jung-Kubiak, T. Reck, N. Llombart, and G. Chattopadhyay, "Beam scanning of silicon lens antennas using integrated piezomotors at submillimeter wavelengths," *IEEE Trans. Terahertz Sci. Technol.*, vol. 9, no. 1, pp. 47–54, Jan. 2019.

[25] R. Ozzola, C. Tadolini, E. A. Speksnijder, and A. Neto, "Full-wave lens antenna analysis with the proxy sources method," *IEEE Trans. Antennas Propag.*, vol. 73, no. 8, pp. 6014–6019, Aug. 2025.

[26] M. Ettorre, A. Neto, G. Gerini, and S. Maci, "Leaky-wave slot array antenna fed by a dual reflector system," *IEEE Trans. Antennas Propag.*, vol. 56, no. 10, pp. 3143–3149, Oct. 2008.

[27] C. A. Balanis, *Advanced Engineering Electromagnetics*. Hoboken, NJ, USA: Wiley, 1989, ch. 11, pp. 571–574.

[28] E. Gandini, A. Tamminen, A. Luukanen, and N. Llombart, "Wide field of view inversely magnified dual-lens for near-field submillimeter wavelength imagers," *IEEE Trans. Antennas Propag.*, vol. 66, no. 2, pp. 541–549, Feb. 2018.

Dunja Lončarević (Graduate Student Member, IEEE) received the B.Sc. degree in electrical engineering from the University of Belgrade, Belgrade, Serbia, in 2020, and the M.Sc. degree in electrical engineering from the Delft University of Technology, Delft, The Netherlands, in 2022, where she is currently pursuing the Ph.D. degree with the Terahertz Sensing Group.

Her research interests include the design of leaky wave antennas, integrated lens antennas, and artificial dielectrics for the next-generation communication and sensing systems.

Martí Xargay Ferrer (Graduate Student Member, IEEE) received the B.Sc. degree in telecommunications engineering from the Technical University of Catalonia (UPC), Barcelona, Spain, in 2023, and the M.Sc. degree (cum laude) in electrical engineering from the Delft University of Technology, Delft, The Netherlands in 2025, where he is currently pursuing the Ph.D. degree with the Terahertz Sensing Group.

His focus is on scanning lens arrays for high-frequency automotive radar applications. His research interests include quasioptical systems, integrated lens antenna arrays, and radar technologies.

Huasheng Zhang (Member, IEEE) received the B.Eng. degree (cum laude) in electronic information engineering from Beihang University, Beijing, China, in 2016, and the M.Sc. (cum laude) and Ph.D. degrees in electrical engineering from the Delft University of Technology, Delft, The Netherlands, in 2018 and 2024, respectively.

His research interests include analyzing and designing leaky wave antennas, lens antennas, photoconductive antennas, and quasioptical systems at millimeter- and submillimeter-wave lengths, and high-frequency electromagnetic analysis techniques.

Andrea Neto (Fellow, IEEE) received the Laurea degree (summa cum laude) in electronic engineering from the University of Florence, Florence, Italy, in 1994, and the Ph.D. degree in electromagnetics from the University of Siena, Siena, Italy, in 2000.

Part of his Ph.D. degree was developed at the European Space Agency Research and Technology Center, Noordwijk, The Netherlands. He was with the Antenna Section, European Space Agency Research and Technology Center, for more than two years. From 2000 to 2001, he was a Post-Doctoral Researcher with the California Institute of Technology, Pasadena, CA, USA, where he was with the Submillimeter-Wave Advanced Technology Group. From 2002 to 2010, he was a Senior Antenna Scientist with TNO Defense, Security, and Safety, The Hague, The Netherlands. In 2010, he became a Full Professor of applied electromagnetism with the Department of Electrical Engineering, Mathematics and Computer Science, Delft University of Technology, Delft, The Netherlands, where he formed and leads the THz Sensing Group. His research interests include the analysis and design of antennas with an emphasis on arrays, dielectric lens antennas, wideband antennas, EBG structures, and THz antennas.

Dr. Neto is a member of the Technical Board of the European School of Antennas and the Steering Committee of the Network of Excellence NEWFOCUS, dedicated to focusing techniques in millimeter- and submillimeter-wave regimes. He is an organizer of the course on antenna imaging techniques. He was a recipient of the European Research Council Starting Grant to perform research on advanced antenna architectures for THz sensing systems in 2011, the H. A. Wheeler Award for the best applications paper of 2008 in the IEEE Transactions on Antennas and Propagation, the Best Innovative Paper Prize of the 30th ESA Antenna Workshop in 2008, and the Best Antenna Theory Paper Prize of the European Conference on Antennas and Propagation in 2010. He was an Associate Editor for IEEE TRANSACTIONS ON ANTENNAS AND PROPAGATION from 2008 to 2013 and IEEE ANTENNAS AND WIRELESS PROPAGATION LETTERS from 2005 to 2013.

Nuria Llombart (Fellow, IEEE) received the master's degree in electrical engineering and the Ph.D. degree in electromagnetics from the Polytechnic University of Valencia, Valencia, Spain, in 2002 and 2006, respectively.

During her master's degree studies, she spent one year with the Friedrich Alexander University of Erlangen-Nuremberg, Erlangen, Germany, and worked with the Fraunhofer Institute for Integrated Circuits, Erlangen. From 2002 to 2007, she was with the Antenna Group, TNO Defense, Security and Safety Institute, The Hague, The Netherlands, working as a Ph.D. student and afterward as a Researcher. From 2007 to 2010, she was a Post-Doctoral Fellow with the Submillimeter-Wave Advanced Technology Group, Jet Propulsion Laboratory, California Institute of Technology, Pasadena, CA, USA. She was a "Ramon y Cajal" Fellow with the Optics Department, Complutense University of Madrid, Madrid, Spain, from 2010 to 2012. In 2012, she was with the THz Sensing Group, Technical University of Delft, Delft, The Netherlands, where she has been a Full Professor since 2018. She has co-authored more than 200 journal and international conference contributions in the areas of antennas and terahertz systems.

Dr. Llombart serves as a Board Member of the International Society of Infrared, Millimeter, and Terahertz Waves. In 2019, she was appointed an IEEE Fellow for contributions to millimeter- and submillimeter-wave quasioptical antennas. She was the co-recipient of the H. A. Wheeler Award for the Best Applications Paper of 2008 in IEEE Transactions on Antennas and Propagation, the 2014 THz Science and Technology Best Paper Award of the IEEE Microwave Theory and Techniques Society, and several NASA awards. She was also the recipient of the 2014 IEEE Antenna and Propagation Society Lot Shafai Mid-Career Distinguished Achievement Award. In 2015, she was the recipient of a European Research Council Starting Grant. Since 2023, the Editor in Chief of IEEE TRANSACTIONS ON THZ SCIENCE AND TECHNOLOGY.